

Generation and Separation of Mesoscale Eddies from Surface Ocean Fronts

GEORGY E. MANUCHARYAN AND MARY-LOUISE TIMMERMANS

Department of Geology and Geophysics, Yale University, New Haven, Connecticut

(Manuscript received 2 May 2013, in final form 6 September 2013)

ABSTRACT

This study is motivated by Arctic Ocean observations of sub-mixed layer eddies found at large distances from their assumed formation region of a surface ocean front. Eddy formation is explored through high-resolution numerical simulations of surface fronts, separating two mixed layers, with a range of configurations similar to those observed in the Arctic Ocean. This study finds that frontal instabilities lead to the development of self-propagating dipoles, which have the potential to propagate far from the front if interactions with other eddies are avoided. However, most dipoles are unbalanced, consisting of a dominating surface cyclone and a weaker anticyclone below, and thus propagate on curved trajectories with eventual re-circulation back to the front. Their maximum separation distance from the front depends on the ratio of self-advecting velocities ϵ ; balanced dipoles that have $\epsilon \approx 1$, and the ability to propagate far from the front. For dipoles generated numerically, this study estimates ϵ using analytical solutions of a $2\frac{1}{2}$ -layer quasigeostrophic model for Gaussian vortices. The distribution of the ratio ϵ for these dipoles is found to be skewed toward higher values (i.e., cyclones are dominant in dipoles). Sensitivity experiments suggest that shallow fronts that separate mixed layers of approximately equal depths favor the development of balanced dipoles that can self-propagate over long distances.

1. Introduction

Instabilities associated with strong upper-ocean fronts can produce eddies that lead to significant vertical and lateral property exchanges. Many observational and numerical studies have examined these frontal dynamics, associated eddy formation, and cross-front exchanges (e.g., Spall 1995; Spall and Chapman 1998; Lee et al. 2006; Boccaletti et al. 2007; Thomas et al. 2008; Thomas 2008; Herbette et al. 2004). Spall (1995) formulated a mechanism for eddy formation at meandering upper-ocean fronts, with low-potential vorticity (PV) water on the dense side of the front. When the front accelerates downstream, a compensating ageostrophic cross-front flow results. The ageostrophic flow will be convergent on the dense side of the front, and, by conservation of mass, a deep cross-front flow will arise from the dense to the light side in the subsurface layer below the front. Parcels subducted from a deep surface layer will be characterized by anomalously low PV and anticyclonic circulation to compensate for compression. This process typically

forms a dipole, with anticyclonic vorticity driven by compression and cyclonic vorticity driven by stretching in the upper layer as fluid is carried away from the front (e.g., Spall 1995). Such dipoles have the ability to self-propagate and can transport anomalous water properties away from the front. Hogg and Stommel (1985) termed a pair of upper- and lower-layer eddies of opposite sign a “heton” because of the self-propagating pair’s ability to transport heat. Spall and Chapman (1998) formulated a theoretical relationship between the magnitude of eddy density flux across a surface front and the frontal parameters, under the assumption that the transport is produced by baroclinic eddy pairs [see also Pedlosky (1985)]. They argue that this flux is proportional to the self-propagation speed of the dipole; their numerical model results confirm that cross-front exchanges are mainly via self-propagating eddy pairs. Hetons are also known to play an important role in transferring heat away from localized convection regions (Legg and Marshall 1993; Legg et al. 1996) and have been observed to form at oceanic boundary currents (Morel and McWilliams 2001; de Ruijter et al. 2004; Ahlnäs et al. 1987; Carton 2001, 2010; Chérubin et al. 2007) and generated in laboratory experiments in stratified flows (e.g., van Heijst and Flor 1989; van Heijst

Corresponding author address: Georgy Manucharyan, 210 Whitney Ave., Kline Geology Laboratory, New Haven, CT 06511.
E-mail: georgy.manucharyan@yale.edu

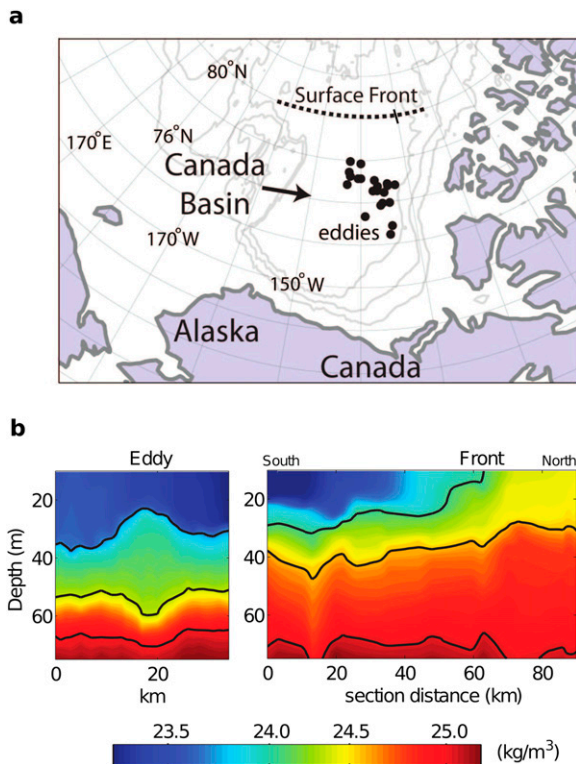


FIG. 1. (a) Map of the Arctic Ocean's Canada Basin, showing the location of a surface front (dotted line) and the location of the sub-mixed layer eddies (dots) studied by Timmermans et al. (2008); the eddies are exclusively anticyclones and are believed to originate at the front. Note that the uneven distribution of eddies in the southern Canada Basin reflects the distribution of water-column profiles. (b) Cross sections of potential density (anomaly from 100 kg m^{-3} referenced to the surface) through a typical eddy and perpendicular to the surface front [modified from Timmermans et al. (2008); data are from ice-tethered profilers [www.whoi.edu/itp; Krishfield et al. (2008); Toole et al. (2011)]].

and Clercx 2009; Voropayev et al. 1991; Stern and Whitehead 1990; Flierl et al. 1983) and 2D soap films (e.g., Couder and Basdevant 1986).

The analysis in this paper is motivated by an observational study of mesoscale eddies in the Arctic Ocean that are believed to be generated by the instability of an upper-ocean front (Timmermans et al. 2008). Timmermans et al. (2008) analyzed ocean temperature and salinity measurements beneath sea ice cover to identify a large number of energetic anticyclonic eddies located immediately below the mixed layer (in the upper-Arctic halocline) in the Arctic Ocean's Canada Basin (Fig. 1a). The anticyclones have typical diameters of about 10 km (Fig. 1b), and strong azimuthal velocities, up to around 30 cm s^{-1} . The anomalous water mass signature of the Arctic eddies suggests that they are generated at a surface density front observed around $\sim 80^\circ\text{N}$ and

extending approximately in the zonal direction (Fig. 1a). The density front separates two distinct water masses: a relatively lower-density (fresh) and shallow mixed layer to the south, and a relatively higher-density (salty) and deep mixed layer to the north (Fig. 1b). Note that the surface of the Arctic Ocean beneath sea ice is mostly at the freezing temperature, so the cooler mixed layer is to the north. Timmermans et al. (2008) argue that the mechanism leading to the generation of the anticyclones is consistent with the mechanism outlined by Spall (1995).

The sub-mixed layer eddies studied by Timmermans et al. (2008) are observed at great distances away from the front where they are purported to originate—up to 500 km (Fig. 1a). The mechanisms that are responsible for such a separation are not understood as observations in this region are limited. Here, we propose that eddies move away from the front as self-propagating dipoles and we examine the conditions under which this is possible. Through high-resolution numerical simulations and idealized analytical models, we examine eddy formation at unstable upper-ocean fronts, and most importantly, the conditions under which eddies could propagate away from the originating front.

The paper is outlined as follows. In the next section we describe the numerical model employed to simulate frontal instability and eddy formation, and consider initial frontal configurations appropriate for the Arctic case. In section 3, we describe frontal instabilities, slumping, and eddy formation, demonstrating the possibility that self-propagating dipoles can propagate away from a slumping front. In section 4, we explore the dynamics of dipole self-propagation and derive an analytical expression for the maximum distance a dipole could travel away from its formation site. The radius of a self-propagating dipole trajectory depends critically on the ratio ϵ of translation velocities of each vortex in the dipole. Section 5 examines the probability of generation of nearly balanced dipoles (i.e., $\epsilon \approx 1$), which can self-advect far from the front. In section 6, guided by the idealized model predictions, we examine the relationship between initial frontal parameters and the properties of dipoles generated. Results are summarized and discussed in section 7.

2. Numerical model setup

The instability of an idealized surface front is simulated numerically with the MIT general circulation model (Adcroft et al. 2013). This is a primitive equation ocean model, which we use in its hydrostatic formulation. An f -plane approximation is used for all but one experiment; the β effect (due to the curvature of the

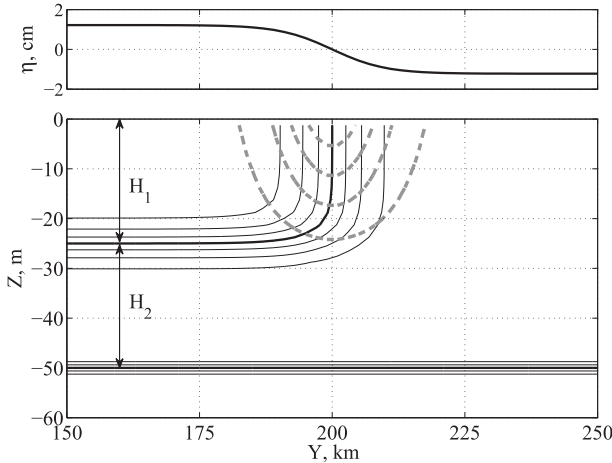


FIG. 2. Schematic illustrating an initial frontal configuration, approximately corresponding to the Arctic front (Fig. 1). (top) The elevation of the free surface (i.e., η) across the front. (bottom) Black contours showing isopycnals spaced by 0.125 kg m^{-3} ; the two thick black contours are isopycnals $\rho_1 = 23.5$ and $\rho_2 = 24.25 \text{ kg m}^{-3}$ (anomalies from 1000 kg m^{-3}) and the dashed contours denote the alongfront velocity with 2 cm s^{-1} contour spacing and a maximum contour of 7 cm s^{-1} .

earth) is negligible at the high latitudes of interest. The model domain is a rectangular prism with dimensions 300 km by 400 km in the horizontal, and 400 m in the vertical. The horizontal resolution of the model is 0.5 km and it has 28 levels in the vertical, with resolution varying from 2.5 m at the surface to 200 m at the bottom. The high resolution is required to resolve mesoscale dynamics with typical values for the deformation radius of the first baroclinic mode throughout our experiments ranging from about 3 to 10 km. Horizontal boundary conditions are periodic in the alongfront direction (x direction), with free slip and no buoyancy flux at the north and south boundaries of the domain. A free-slip condition is applied at the bottom, with no wind or buoyancy forcing at the surface. The simulations presented here model the relaxation of a surface density front from its initial state.

Horizontal viscosity and horizontal tracer diffusivity are set equal to $2 \text{ m}^2 \text{ s}^{-1}$, vertical diffusivity to $10^{-5} \text{ m}^2 \text{ s}^{-1}$, and a biharmonic viscosity to $10^5 \text{ m}^4 \text{ s}^{-1}$ —the minimum values required for numerical stability of the model at a given resolution. We have tested a range of vertical and horizontal resolutions as well as various diffusivities to conclude that the chosen values are sufficient to resolve the relevant processes involved in frontal instability and eddy formation.

a. Initial conditions

The following idealized cross-frontal (y direction) structure is specified as follows (see Fig. 2):

$$\begin{aligned} \rho - \rho_0 = & \frac{\Delta\rho_y}{4} \left[\tanh\left(\frac{-z + H_1}{\delta h}\right) + 1 \right] \\ & \times \left[\tanh\left(\frac{y - L/2}{L_f}\right) - 1 \right] + \Delta\rho_z \mathcal{H}(z - H_1 - H_2) \end{aligned} \quad (1)$$

(see Thomas 2008). Here, L_f is the frontal width; $\Delta\rho_y$ is the density difference across the upper layer (layer 1 of thickness H_1 ; Fig. 2), $\Delta\rho_z$ is the density difference across the underlying layer (layer 2 of thickness H_2 on the light side of the front), and $\rho_0 = 1023 \text{ kg m}^{-3}$ is a reference density; $\delta h = 5 \text{ m}$ is the thickness of the pycnocline separating the layers; L is the domain size in the cross-frontal direction; and \mathcal{H} is the Heaviside step function. The initial frontal structure is uniform in the x direction.

The initial elevation of the free surface η and velocity profiles (U , V) are calculated using the thermal wind balance, and assuming a level of no motion at the bottom of the domain:

$$\eta(y) = \frac{1}{\rho(y, 0)} \int_{-H}^0 \left\{ \rho(y, z) - \frac{1}{2} [\rho(0, z) + \rho(L, z)] \right\} dz, \quad (2)$$

$$U(y, z) = \frac{g}{f} \int_{-H}^z \frac{1}{\rho} \frac{\partial \rho}{\partial y} dz, \quad \text{and} \quad V(y, z) = 0, \quad (3)$$

where f is the Coriolis parameter, and $H = 400 \text{ m}$ is the total depth of the domain. Small-amplitude random perturbations (white noise) are superimposed on the initial density distribution to initiate frontal instability. For each set of initial conditions, we perform at least six simulations with different perturbation field realizations to improve the reliability of eddy statistics. This is an alternative to having a wider model domain in the alongfront direction; with typical frontal meanders having about 10-km-length scales, six experiments allows for the simulation of hundreds of frontal meanders. Numerical calculations are performed for 70 model days (1 day ≈ 2 inertial periods), which is sufficient for the instabilities to substantially run down the front.

The key parameters prescribing the front are $H_{1,2}$, L_f , and $\Delta\rho_y$ ($\Delta\rho_z$ is less important). The relevant nondimensional parameters are

$$\text{Ro} = \frac{g'_1 H_1}{f^2 L_f^2} \quad \text{and} \quad \text{Bu} = \frac{g'(H_1 + H_2)}{f^2 L_f^2}, \quad (4)$$

where the Rossby number Ro (related to the baroclinic component of the flow) characterizes the relative

TABLE 1. Frontal configurations investigated in the numerical experiments with the experiment runs provided in the first column on the rhs. Parameters are defined in the text. Experiment 4β used $\beta = 10^{-11} \text{ s}^{-1} \text{ m}^{-1}$.

	H_1 (m)	H_2 (m)	g'_1 (m s^{-2})	L_f (km)	U_g (cm s^{-1})	Ro	Bu
1	20	30	0.01	10	7.0	0.10	0.25
2	25	30	0.01	10	8.8	0.12	0.25
3	30	20	0.01	10	10.5	0.15	0.25
4β	30	20	0.01	10	10.5	0.15	0.25
5	35	15	0.01	10	12.3	0.17	0.25
6	40	10	0.01	10	14.0	0.20	0.25
7	35	65	0.01	10	12.3	0.17	0.50
8	35	165	0.01	10	12.3	0.17	1.00
9	20	5	0.01	10	7.0	0.1	0.13
10	80	20	0.01	10	28.0	0.4	0.50
11	30	20	0.01	5	21.0	0.6	1.00
12	30	20	0.01	20	5.3	0.04	0.06
13	30	20	0.01	40	2.6	0.01	0.02
14	30	20	0.04	10	42.0	0.15	1.00
15	30	20	0.0025	10	2.6	0.15	0.06

importance of Coriolis to inertial terms in the momentum equation, and the Burger number $\text{Bu} (=R_d^2/L_f^2)$ characterizes the width of the front compared to the baroclinic deformation radius $R_d = \sqrt{g'_1(H_1 + H_2)}/f$ (with reduced gravity $g'_1 = g\Delta\rho_y/\rho_0$). The remaining dimensionless parameter is the frontal aspect ratio $(H_1 + H_2)/L_f$.

For the Arctic front (Fig. 1b), $g'_1 \approx 0.01$, $H_1 \approx 30$ m, $H_2 \approx 20$ m, $f = 1.4 \times 10^{-4} \text{ s}^{-1}$, and $L_f \approx 10$ km, giving $\text{Ro} \approx 0.15$, $\text{Bu} \approx 0.25$, and $R_d \approx 5$ km (experiment 3; Table 1). In section 6, we investigate whether and how the properties of generated dipoles depend on the initial frontal configuration by simulating the evolution for a range of initial conditions as outlined in Table 1.

b. Methods

We approximate the three-dimensional output of the numerical model as three two-dimensional layers. The layers are separated by isopycnals: 23.5 and 24.25 kg m^{-3} (Fig. 2), except for experiments 14 and 15 (Table 1). Note that the thickness of the bottom layer is relatively large and for simplicity of the analysis, we consider it to be motionless (i.e., $2\frac{1}{2}$ -layer dynamics). For a given layer, we calculate its thickness h and the vertically averaged velocity field (\bar{U}, \bar{V}) in the layer. This is similar to splitting the fluid motion into contributions from the first and second baroclinic modes. In numerical experiments the vertical stratification is diffusing with time, thus slightly altering the vertical structure of the baroclinic modes; however, its general shape is preserved making the splitting into layers a useful simplification.

We use these two-dimensional velocities, along with layer thicknesses, to compute a diagnostic for the flow dynamics—the potential vorticity Q :

$$Q = \frac{\zeta + f}{h} \quad \text{and} \quad \zeta = \frac{\partial \bar{V}}{\partial x} - \frac{\partial \bar{U}}{\partial y}, \quad (5)$$

where ζ is the relative vorticity. The analytical model of eddies presented in section 4 uses the linear quasigeostrophic equations, and the linearized version of the PV anomaly with respect to the background is computed as

$$Q' = \frac{\zeta}{\bar{h}} - \frac{fh'}{\bar{h}^2}, \quad (6)$$

where \bar{h} represents the mean layer thickness of the surrounding fluid, and h' is the perturbation from that mean.

On short time scales, dissipative processes such as momentum and tracer diffusivity have a negligible effect on the first-order dynamics, and the subducted parcels preserve their initial PV thus making this quantity a suitable water mass tracer (see, e.g., Spall 1995). On time scales on the order of months, vertical diffusivity acts to dissipate the PV anomalies associated with eddies.

3. Frontal instabilities and dipole formation

a. Slumping

We begin with a description of the evolution of the front as the model progresses (Fig. 3). Instabilities and eddies release potential energy and slump the front. After ~ 20 inertial periods (IPs) from the beginning of the simulation instabilities with the shortest resolved wavelengths are observed, these grow to form eddies that are generated on top of slower-growing mesoscale instabilities having length scales of a few tens of kilometers (see, e.g., Stone 1966; Boccaletti et al. 2007; Fox-Kemper et al. 2008; Lapeyre et al. 2006; Sakai 1989). At about 50 IP, the mesoscale instabilities are fully developed while the smaller scales are mostly absent (Fig. 3). An inverse cascade of energy to larger scales (Rhines 1979; Smith and Vallis 2001) is clearly present in the simulations (Fig. 4a), with the length scales of the dominant perturbations increasing linearly with time (Fig. 4b). The increase in length scale of the dominant perturbations is a result of two processes: merger of eddies of the same vorticity sign (Fig. 4c) and the fact that longer wavelength meanders have slower growth rates (e.g., Eady 1949). Several studies have addressed the details of dipole–dipole interaction (e.g., Sokolovskiy and Verron 2000; Reinaud and Carton

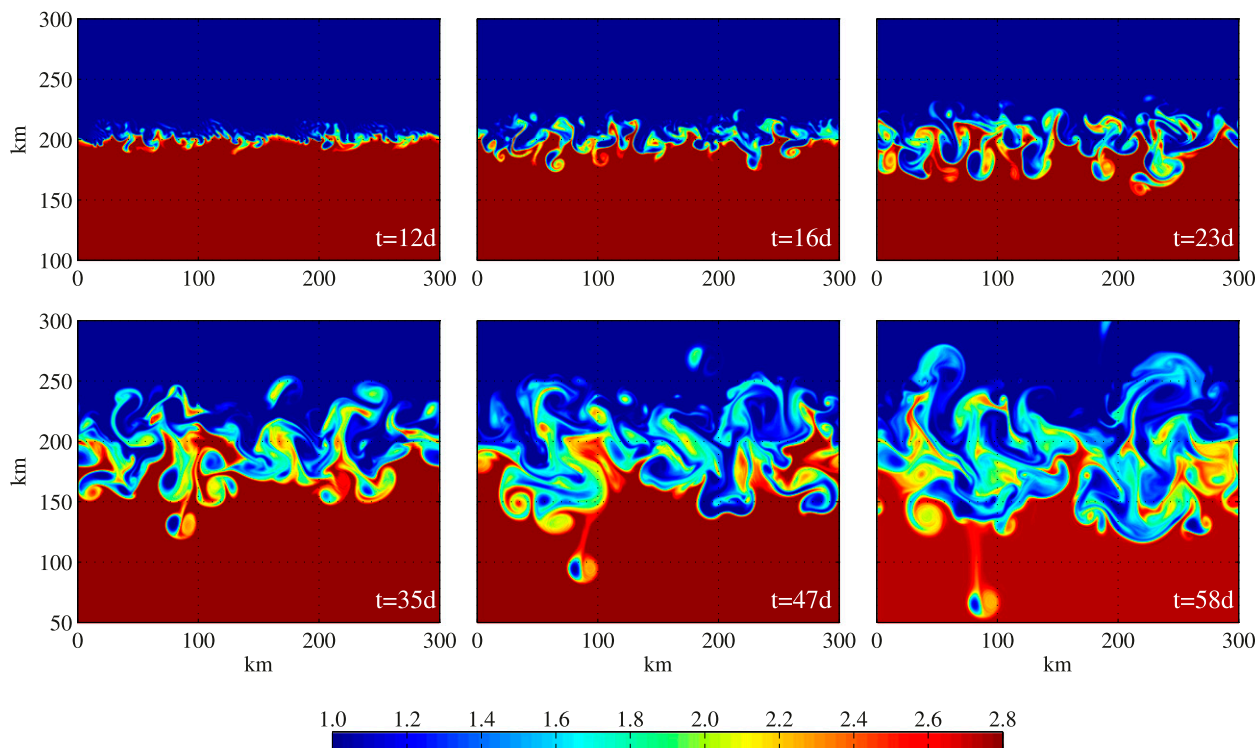


FIG. 3. Plan view of the model domain showing the formation of frontal instabilities as a simulation (with initial conditions corresponding to experiment 5; Table 1) progresses [snapshots are taken on model days: 12, 16, 23, 35, 47, and 58 (1 day \approx 2 IP)]. Colors indicate PV [(5)] in layer 2, normalized by the value on the deep side of the front [$f/(H_1 + H_2)$]. Note the formation of dipoles in the early stages, and later separation of a dipole from the front.

2009; Voropayev et al. 1991), with dipole instabilities also known to lead to splitting of a single dipole (Reinaud and Carton 2009).

The evolution of the frontal-slumping region (Fig. 4b) is estimated by calculating the width in the cross-front direction of an interval over which the eddy kinetic energy is at least 60% of its maximum value (corresponding to two standard deviations of a Gaussian fit). Initially, the frontal width is larger than the scale of dominant perturbations, corresponding to multiple eddies forming within the frontal region (Fig. 4b). After about 10 days, the frontal width is the same size as the scale of dominant eddies and the two grow at the same rate. The width increases with time almost linearly, which corresponds to growth of the energetic area by merger of vortex dipoles [see Carton (2001), and references therein]. The slumping speed poses a significant constraint on the probability of eddy detachment from the front as slow-moving eddies are likely to be reincorporated into the front. This is addressed in section 6.

b. Dipole formation

The simulations show dipoles to be common features, which are easily identified as PV anomalies of opposite

sign located in different layers and shifted horizontally from each other (Figs. 5 and 6). In the early stages of growth of a frontal meander, layer 1 meanders at a distinctly smaller scale than layer 2; the ratio of scales is approximately proportional to the ratio of the first to second baroclinic deformation radii (see appendix). The layer-1 meander is offset to the right (east) side of the layer-2 meander, in the direction of the vertical shear of the mean front. The layer-1 grows faster than the layer-2 meander and forms a cyclone by pinching off from the strongly elongated high-PV anomaly water mass. At the same time, the layer-2 meander grows and as it penetrates the shallow side of the front it develops anticyclonic vorticity. At this stage, the cyclone in layer 1 has developed a cyclonic flow field in layer 2 that advects the anticyclone away from the front [this process of self-advection of dipole pairs is known as the “hetonic mechanism” (see, e.g., Gryanik 1983; Gryanik et al. 2006; Hogg and Stommel 1985)]. Note that the upper-layer cyclone must be offset horizontally from the lower-layer anticyclone in the direction of the mean flow, otherwise the hetonic mechanism would damp the perturbation. Ultimately, the layer-2 meander becomes sufficiently elongated that the anticyclone also pinches

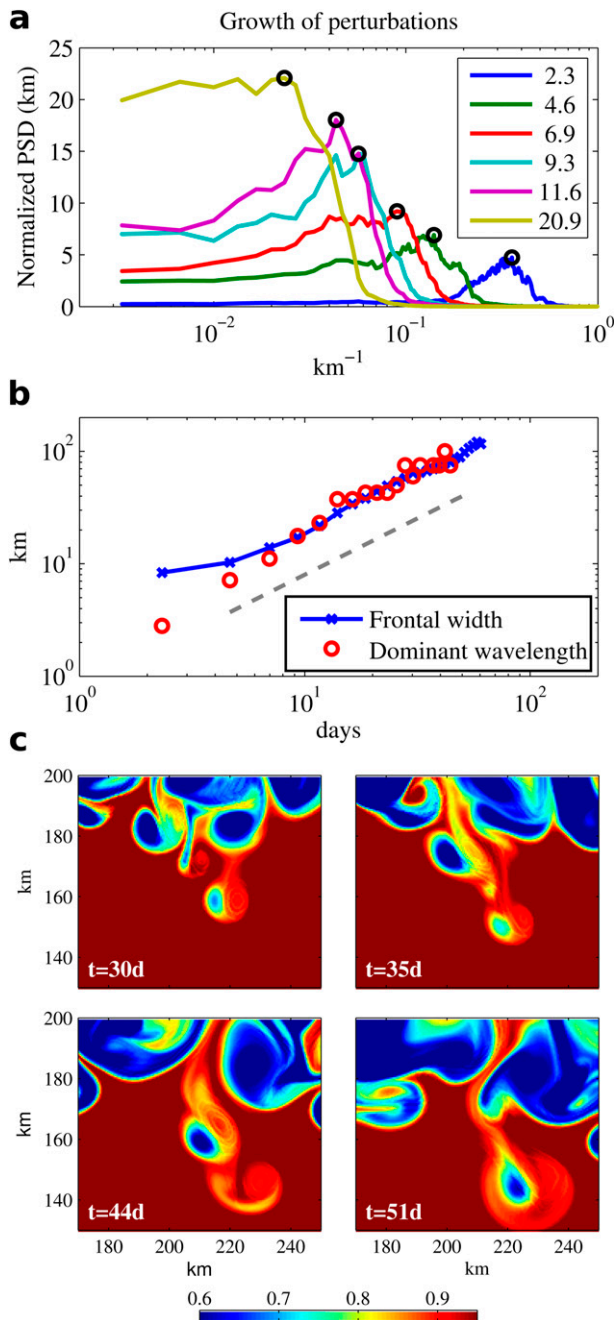


FIG. 4. (a) Time evolution of the normalized power spectral density of the free-surface height anomaly along the front. The legend shows time (days) and circles denote the dominant wavenumber. (b) Frontal width (blue) and the dominant perturbation scale (red) vs time. (c) Time sequence of PV anomaly in layer 2 demonstrating the growth of separated eddies through mergers corresponding to days 30, 35, 44, and 51 for the experiment shown in Fig. 3.

off. After separation from the front, the PV anomalies that constitute each eddy adjust to the flow field associated with these anomalies through nonlinear advection to eventually form a pair of coherent stable vortices.

Figure 6 illustrates how the cyclone (positive PV anomaly in layer 1) originates within the frontal outcropping region (having very high PV) while the anticyclone (negative PV anomaly in layer 2) originates on the deep (low PV) side of the front. There is a signature of a weaker anticyclone located directly below the cyclone. The anticyclonic PV anomaly is created because of a diffusive spin down of the relative vorticity in the second layer generated from a cyclone in a first layer. The magnitude of this effect can be reduced by decreasing horizontal viscosity, although at the expense of increasing the model resolution.

The majority of dipoles observed in the numerical experiments do not evade the influences of the slumping front and inverse cascade. Most dipoles generated by the instability recirculate back to the front because of their curved trajectories and the increasing frontal width. There are cases, however, where a dipole is observed to escape the frontal influence (e.g., bottom right in Fig. 3). The observed self-propagation speed of the detached dipole in Fig. 3 is $\sim 4 \text{ cm s}^{-1}$ [corresponding to about $100 \text{ km (month)}^{-1}$]. Attention is focused here on eddies advected from the side of the front with the deep mixed layer to the shallower side as these are the eddies relevant to the Arctic Ocean. While numerical simulations show eddies forming on the deeper side of the front, these are surface-intensified features and hence would be dissipated rapidly by mixing processes either of frictional origin due to winds and the motion of sea ice or due to convection arising from surface buoyancy fluxes. The sub-mixed layer anticyclones on the shallow side of the front are likely to be preserved for longer times as they are insulated from surface processes by the strong stratification at the base of the mixed layer. We hypothesize here that dipole self-propagation is the key to understanding the shallow anticyclones observed in the Arctic Ocean. In the following sections, we examine what dipole characteristics favor their escape from the frontal region and whether there are particular frontal configurations that lead to enhanced production of separated dipoles.

4. Dipole trajectories

Dipoles are composed of the two dominant PV anomalies (cyclonic in layer 1 and anticyclonic in layer 2), shifted horizontally by a distance Δ of about one eddy radius (e.g., Fig. 5). This induces a self-propagation that can be understood in terms of interactions between the two vortices—the core of the first vortex is advected by the velocity field induced by the second vortex and vice versa (e.g., Saffman 1992). While much progress has been made in understanding the dynamics of dipoles [see

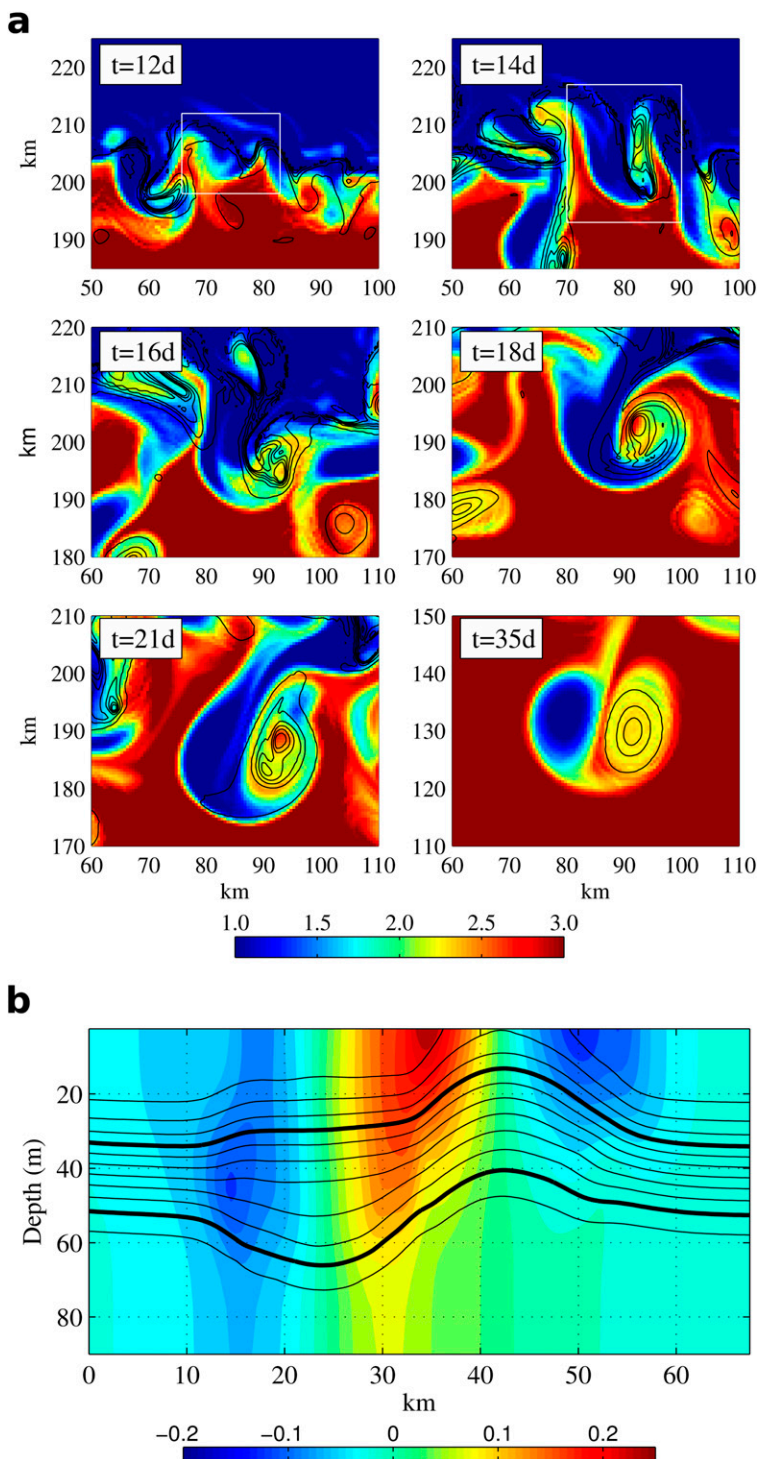


FIG. 5. (a) PV field in layers 1 (black contours) and 2 (colors) showing the time evolution of frontal meanders leading to production of a typical dipole corresponding to model days 12, 14, 16, 18, 21, and 35, respectively (Fig. 3). (b) Vertical section through the center of a typical dipole that clearly escaped the influence of its originating front (Fig. 3; model day 47). Colors indicate speed (m s^{-1}) perpendicular to the section, and contours are isopycnals (with spacing 0.125 kg m^{-3}). Note the effects of vertical mixing as compared to the initial configuration.

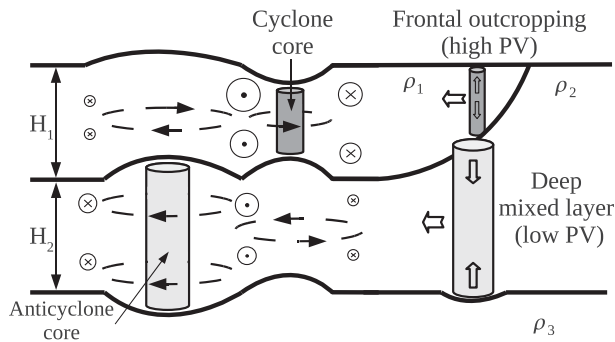


FIG. 6. Schematic of dipole formation indicating the water mass origins of the cyclone and anticyclone.

Carton (2001), and references therein], here we develop a specific formalism that allows us to interpret and analyze modeled frontal instabilities in the context of dipole trajectories.

a. Kinematics

To calculate dipole trajectories, consider the constant translation velocities of each vortex in the dipole U_i (for $i = 1, 2$), defined positively for a cyclone–anticyclone pair as in Fig. 7. The propagation velocities are directed perpendicular to the line connecting the centers of the vortices and thus the separation distance between the vortices Δ does not change in time. The kinematic equations describing the time evolution of center positions $\mathbf{r}_i = (x_i, y_i)$ of the vortices are as follows:

$$\dot{\mathbf{r}}_1 = \frac{U_1}{\Delta} \mathbf{k} \times (\mathbf{r}_2 - \mathbf{r}_1) \quad \text{and} \quad (7)$$

$$\dot{\mathbf{r}}_2 = \frac{U_2}{\Delta} \mathbf{k} \times (\mathbf{r}_2 - \mathbf{r}_1). \quad (8)$$

Combining these equations yields an oscillator equation for the separation distance between vortices

$$(\mathbf{r}_2 - \mathbf{r}_1)'' + \omega^2(\mathbf{r}_2 - \mathbf{r}_1) = 0, \quad (9)$$

where frequency $\omega = (U_2 - U_1)/\Delta$. Thus, in a reference frame moving with one vortex the other vortex rotates around it and vice versa; in the special case of balanced vortices (i.e., $U_1 = U_2$) they move parallel to each other.

It is useful to define the coordinate of a self-propagating dipole (the same sign for U_1 and U_2) as

$$\mathbf{r}_c = \frac{U_2 \mathbf{r}_1 + U_1 \mathbf{r}_2}{U_1 + U_2}, \quad (10)$$

where \mathbf{r}_c lies between the two eddies and is an analog of the center of vorticity for two-dimensional point dipoles. Its derivative with respect to time defines a dipole

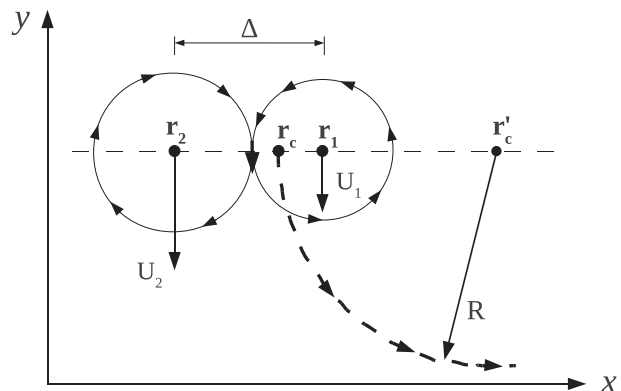


FIG. 7. Schematic indicating the parameters of the dipole. Symbols shown are as defined and used in the text.

translation speed $U_d = 2U_1U_2/(U_1 + U_2)$. Obtaining a solution for $\mathbf{r}_{1,2}$ for an example dipole with a cyclone and anticyclone initially at $(0, 0)$ and $(\Delta, 0)$, respectively, we find that the dipole center propagates on a circular path with coordinates

$$\mathbf{r}_c - \mathbf{r}'_c = 2\Delta \frac{U_1U_2}{U_2^2 - U_1^2} \begin{pmatrix} -\cos \omega t \\ -\sin \omega t \end{pmatrix}, \quad (11)$$

where \mathbf{r}'_c is the center of a circle (Fig. 7). Therefore, the radius of a dipole trajectory R depends critically on the ratio of vortex propagation velocities ϵ :

$$R = \frac{2\Delta}{\left| \epsilon - \frac{1}{\epsilon} \right|} \quad \text{and} \quad \epsilon = \frac{U_2}{U_1}. \quad (12)$$

The derivation is not only valid for U_1 and U_2 constant in time, but also for cases where their ratio ϵ is constant in time, because the time dependency can be incorporated into a rescaled time variable. In this case, the dipole would move along a circular trajectory with a time-dependent velocity. This proves to be a useful result as we observe that the dipole vortices decay in time (because of diffusion and entrainment) at a similar rate such that ϵ remains relatively constant.

The radius of the trajectory varies strongly in the region of $\epsilon \approx 1$ where the dipole trajectory is essentially a straight line in our finite domain (e.g., Fig. 3, bottom right). However, for values of $\epsilon > 1.6$ (or $\epsilon < 0.6$) the radius becomes less than twice the separation distance Δ . In this case, the dipole has a strongly curved trajectory, and takes little time to propagate back to its originating front and be engulfed. The circular trajectories of dipoles are clearly observed in our numerical simulations, and these paths lead to the majority of initially detached dipoles being reabsorbed by the front. Thus, the value of ϵ poses a strong constraint on the probability for dipole escape far from the front (i.e., $R \gg \Delta$).

Because it is not possible to split the velocity field obtained from the numerical model into advecting contributions from each of the two eddies in a dipole, we proceed by developing an idealized dynamical model of the dipole flow field based on PV anomalies of each of the two eddies. Our aim is to identify factors controlling the ratio of self-propagating velocities ϵ .

b. Dynamics

It is intuitive that for a given dipole its ratio ϵ should be determined by the relative strength of the cyclone and anticyclone as well as the stratification parameters of the ambient fluid. We thus proceed to derive this relationship using a quasigeostrophic set of equations (Pedlosky 1982; Vallis 2006), which is sufficient to represent the essential dynamical features of dipoles (see, e.g., Polvani 1991; Flierl et al. 1980; Flierl 1987; Carton 2001; Swaters 1995). Here, we assume 2½-layer dynamics (i.e., two active layers and a bottom stationary layer) with eddies in a dipole represented as delta functions of PV anomalies with magnitudes $S_{1,2}$ (the point vortex assumption is relaxed later). We further simplify by considering the linear quasigeostrophic equations with the rigid-lid approximation:

$$\nabla^2\psi_1 + F_1(\psi_2 - \psi_1) = S_1\delta(\mathbf{r}_1) \quad \text{and} \quad (13)$$

$$\nabla^2\psi_2 + F_2(\psi_1 - \psi_2) - F_3\psi_2 = S_2\delta(\mathbf{r}_2), \quad (14)$$

where $\psi_{1,2}$ are the streamfunctions for layers 1 and 2, respectively, and $\mathbf{r}_1 - \mathbf{r}_2 = \mathbf{\Delta}$. The stratification parameters are

$$F_1 = \frac{f^2}{g'_1 H_1}, \quad F_2 = \frac{f^2}{g'_2 H_2}, \quad \text{and} \quad F_3 = \frac{f^2}{g'_2 H_2}, \quad (15)$$

where g'_1 and g'_2 denote reduced gravity corresponding to the density difference across the base of layers 1 and 2, respectively. It is useful to split the solution to this equation into two contributions: the circulation $u_2(r)$ that arises in layer 2 because of the vortex in layer 1 that advects the core of the vortex in layer 2, and similarly the circulation $u_1(r)$ (see the appendix). These velocities are found to be

$$u_2(r) = -S_1 F_2 \frac{K_1(r/\lambda_1)/\lambda_1 - K_1(r/\lambda_2)/\lambda_2}{\lambda_2^{-2} - \lambda_1^{-2}} \quad \text{and} \quad (16)$$

$$u_1(r) = S_2 F_1 \frac{K_1(r/\lambda_1)/\lambda_1 - K_1(r/\lambda_2)/\lambda_2}{\lambda_2^{-2} - \lambda_1^{-2}}, \quad (17)$$

where K_1 is the first-order modified Bessel function of the second kind, and $\lambda_{1,2}$ are the first and second

baroclinic deformation radii (defined in the appendix). Bessel functions appear in the solutions because the equation for the baroclinic mode involves a Laplacian operator in cylindrical coordinates. In a special case of $F_3 = 0$, the equation becomes equivalent to a 2-layer system and would have a barotropic mode with a logarithmic streamfunction profile ($1/r$ velocity decay). In the case of point vortices, the functional dependence of the propagating velocities is the same. Note that for point vortices $U_i = u_i(r = \Delta)$. This allows for a simple relation for their ratio

$$\epsilon = \frac{S_1 H_1}{S_2 H_2}. \quad (18)$$

Thus, for a dipole to propagate far from the front (ϵ close to unity), its cyclone and anticyclone components should be balanced in strength expressed in terms of their PV anomalies scaled by the mean layer thicknesses.

The relation (18) is obtained for point vortices and provides useful insights; however, numerical simulations show that PV anomalies of each eddy in a dipole are better represented with a Gaussian profile (Fig. 8a). Radially symmetric Gaussian PV anomalies allow for simplifications and the use of Hankel transformations to obtain streamfunction profiles [(A24) and the appendix]. The analytical model uses the radii and magnitudes of the PV anomalies and a separation distance (i.e., Δ) to obtain the velocity profiles for each dipole. Simulations indicate four PV anomalies (two in each layer) associated with a single dipole, although the dominating effects on the velocity field are due to the cyclone in layer 1 and the anticyclone in layer 2 (Figs. 5b, 6, and 8a). This approximate linear solution agrees reasonably well with the velocity fields of dipoles in the numerical model, with the biggest discrepancies in the regions of overlap between the two vortices in the dipole (Fig. 8). This disagreement likely arises from comparing the 2½-layer theory to motions in a continuously stratified fluid. This is analogous to assuming that all of the motion occurs in the first and second baroclinic modes, which neglects contributions from higher modes. Furthermore, we were able to make use of a fully linearized model by splitting the full velocity field into two contributions, one from the cyclone and the other from the anticyclone. This approximation is likely to have the largest errors in the overlap region, where due to strong currents the nonlinearities in the PV equations are not insignificant. Nevertheless, the analytical model results are useful in that they provide a ratio of self-propagating velocities, essential for assessing the trajectory of a dipole.

If the sizes of cyclone and anticyclone PV anomalies are the same within the Gaussian approximation, the

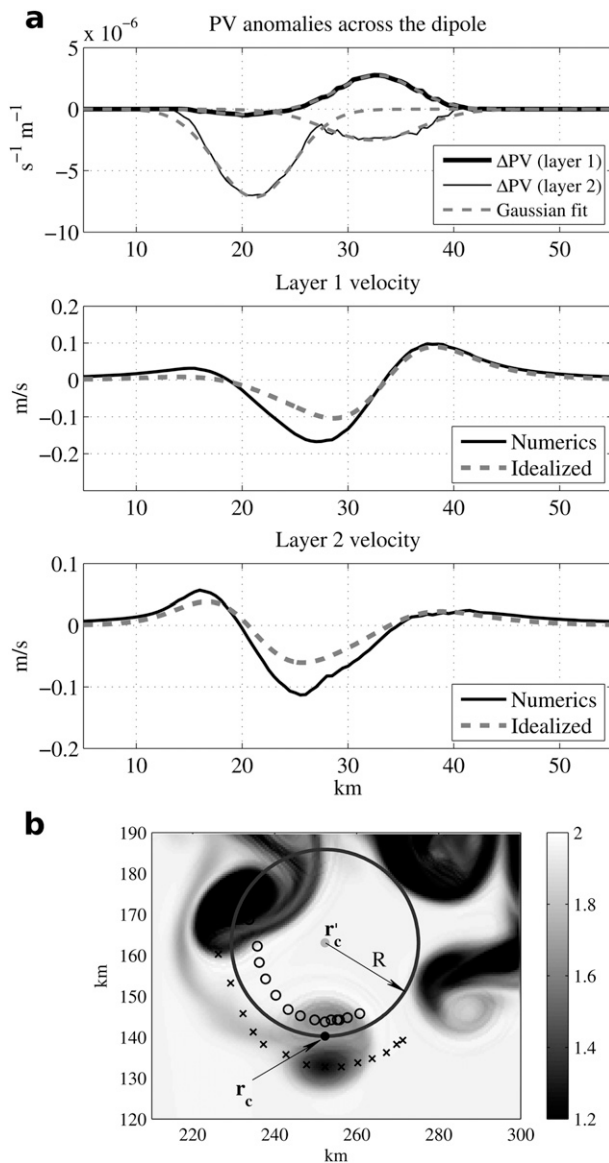


FIG. 8. (a) PV anomalies [(6)] across a dipole in layer 1 and 2, and the corresponding Gaussian fit to individual eddies (black dashed line). Velocity profiles in layers 1 and 2 across a dipole taken from the output of the numerical model (solid black) and calculated using an idealized Gaussian vortex model (dashed gray). (b) An example dipole trajectory (the normalized PV field in layer 2 is shown, the initial conditions are experiment 2; Table 1) with the estimated radius derived from the idealized theoretical model prediction based on the magnitudes of the dipole PV anomalies. The crosses show the path of the anticyclone in layer 2 and the circles show the cyclone in layer 1.

expression for ϵ is identical to that for point vortices [(18)], because the solutions for self-propagating velocities in both layers have the same functional dependence (the appendix). It should be noted that in the non-quasigeostrophic simulations, the average size of a layer-1 cyclone is about 10%–20% smaller than a layer-2

anticyclone because the presence of eddies alters the background vorticity and layer thickness leading to smaller deformation radii for cyclones.

Thus, a combination of the idealized dynamic and kinematic models gives a prediction for the potential propagation distance of a dipole assuming no interactions with the front or other eddies. A comparison of a typical model dipole trajectory to a trajectory predicted by the idealized model based on the observed dipole PV anomalies (Fig. 8b) indicates generally good agreement after the initial stages. Note that dipole trajectories are typically limited to propagate only about a quarter of the circle that defines their propagation before merging with other eddies or frontal meanders.

5. Probability of balanced dipoles

The essential parameters, ϵ and Δ , that determine propagation of a dipole depend upon the characteristics of the particular frontal meander from which the dipole was produced. While it is impossible to predict the dynamics of each frontal meander produced throughout the duration of a model run, progress can be made by assuming that there exists a probability density function (PDF) for the properties of dipoles shed from a front having a specified initial frontal configuration.

The model runs presented in this section are initialized by parameters appropriate for the Arctic case (Fig. 1b and experiment 3 in Table 1). For each model simulation, dipoles are located by making use of the fact that they are composed of vortices with strong PV anomaly maxima and minima in layers 1 and 2, respectively. These PV extrema are offset horizontally by a distance (i.e., Δ), which is of a similar magnitude as the characteristic size of each eddy. For the statistics, we choose only coherent pinched-off dipoles with a life span of at least ~ 5 model days. After identifying prominent dipoles, we fit Gaussian profiles through their PV anomaly fields (e.g., Fig. 8a). In this way, for each dipole we obtain the strengths of the two vortices S_i , their horizontal length scales σ_i , and a separation distance (i.e., Δ). The ratio of velocities (i.e., ϵ) is calculated for each dipole using the analytical solution with the Gaussian fits (see the appendix). For most observed dipoles, ϵ falls between 0.5 and 3, with the PDF centered at ~ 1.5 , implying that there are more eddy pairs where the cyclone dominates (Fig. 9a). The PDF has a long tail in the distribution at large ratios, where the cyclone is several times stronger than the anticyclone. On the small ϵ side, where the anticyclone in a given dipole is stronger than the cyclone, there is a sharp cutoff at $\epsilon \approx 0.6$, implying that there is a limit to the relative strength of an anticyclone in a dipole (Fig. 9a).

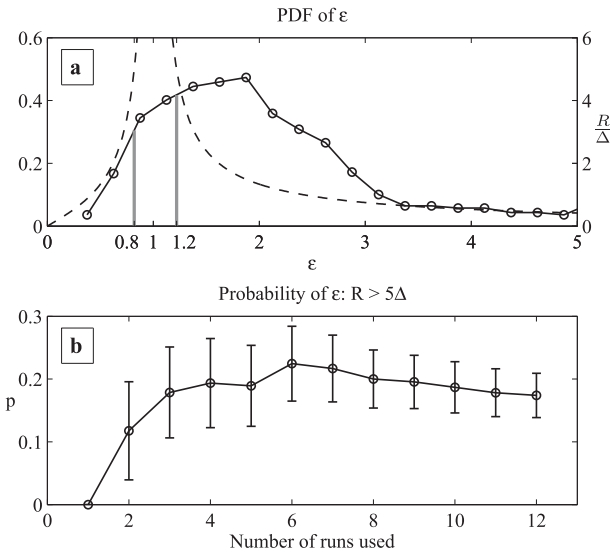


FIG. 9. (a) PDF of ϵ (solid line; left y axis) and dependence of R/Δ on ϵ [(12); dashed line; right y axis]. Bin-size is 0.25. (b) Convergence of the probability of a balanced dipole vs the number of simulations performed. A total of 115 dipoles were identified in an ensemble of 12 model runs for the frontal configuration 3 (Table 1).

The imbalance in strengths of eddies that compose a dipole can be understood by considering the range of possible PV anomalies for the cyclones and anticyclones. The originating front has a top layer that outcrops to the surface and the PV jump across the front can be very large (technically, infinite). This means that water parcels that are transported by meanders from the immediate frontal region to the light side of the front could have very large cyclonic PV anomalies (Fig. 6). On the other hand, in layer 2 there is only a finite PV gradient across the front, which bounds the PV anomaly of an anticyclone: $\Delta PV_{\max} = f(H_1 + H_2) - fH_2$.

The probability of the production of balanced dipoles ($\epsilon \approx 1$) can be assessed by considering, for example, dipoles with $R > 5\Delta$ or $\epsilon \in [0.82 \ 1.22]$ (Fig. 9a). We introduce $p = P(\epsilon: R > 5\Delta)$ as the probability that dipoles are balanced (with unbalanced dipoles having probability $1 - p$), and estimate p as the ratio of the number of balanced dipoles n to the total number of dipoles observed N . The standard deviation of such an estimate is equal to $\sigma_p^2 = p(1 - p)/N$ (assuming that N is sufficiently large for the central limit theorem to apply). The estimated probability is about 0.2 (Fig. 9b), which means that the majority of dipoles are unbalanced and cannot separate far from the front. The probability p has a relatively fast convergence rate; from about 5 to 6 runs (giving a sample size of about 60 dipoles) are sufficient to estimate p with 20%–30% error (Fig. 9b).

Even after a balanced dipole is produced, the probability remains that it will be absorbed by the front because

of interaction with the frontal meanders and other dipoles. Dipole–dipole interactions often lead to mergers and the formation of a larger dipole; however, this mechanism is not efficient enough to increase the dipole survival rate. Thus, eddy separation from the front is a rare event; throughout the range of simulated fronts and different model realizations we have observed only a handful of dipoles that were able to clearly escape the influence of the front. It is notable that escaped dipoles all have $\epsilon \approx 1$. We next proceed to examine whether there are particular frontal configurations that are favorable to the production of balanced dipoles that propagate long distances.

6. Sensitivity of dipole properties to frontal parameters

Here, we explore the dependence of dipole ϵ values on the initial frontal configuration from which they were produced. To begin, we vary the Ro number while keeping the Bu number fixed (experiments 1–6 in Table 1; Fig. 10a). This is achieved by varying H_1 from 20 to 40 m in increments of 5 m, with $H_1 + H_2 = 50$ m and all other parameters fixed. The PDF of ϵ is qualitatively the same across these parameter ranges (Fig. 10a): there is a peak at about $\epsilon = 1.5$, a long tail for values of $\epsilon > 1$, and a sharp cutoff at about $\epsilon = 0.5$. The estimated probability for balanced eddy production (as in Fig. 9b) has no apparent dependency on the Ro number, with variations between runs being within the expected error of the estimate. One of these experiments (experiment 4, Table 1) takes into account the β effect using $\beta = 10^{-11} \text{ s}^{-1} \text{ m}^{-1}$ (corresponding to about 60° latitude; i.e., stronger than for the Arctic front discussed here). Here, dipoles are not significantly affected by westward β drift (e.g., Nof 1981; Killworth 1983) because typical dipole propagation speeds (a few centimeters per second) are much faster than β -induced drift speeds [β drift is approximately equal to the first-mode baroclinic Rossby wave phase speed $\approx \beta R_q^2 \approx 0.025 \text{ cm s}^{-1}$, see Chelton et al. (2011)]. However, for the frontal conditions examined here, the β effect appears to produce a slight bias toward stronger cyclones, thus decreasing the probability of balanced dipoles (Fig. 10a).

The next set of experiments explores the dependency on the Bu number while keeping the Ro number fixed, achieved by varying H_2 and keeping all other parameters fixed (experiments 5, 7, and 8, Table 1; Fig. 10b). Increasing H_2 (i.e., increasing Bu) decreases the relative PV difference across the front in layer 2, and reduces the strength of anticyclones in layer 2. The PV distribution in layer 1 remains the same, with high values in the outcropping region. As a result, for a larger Bu, there is

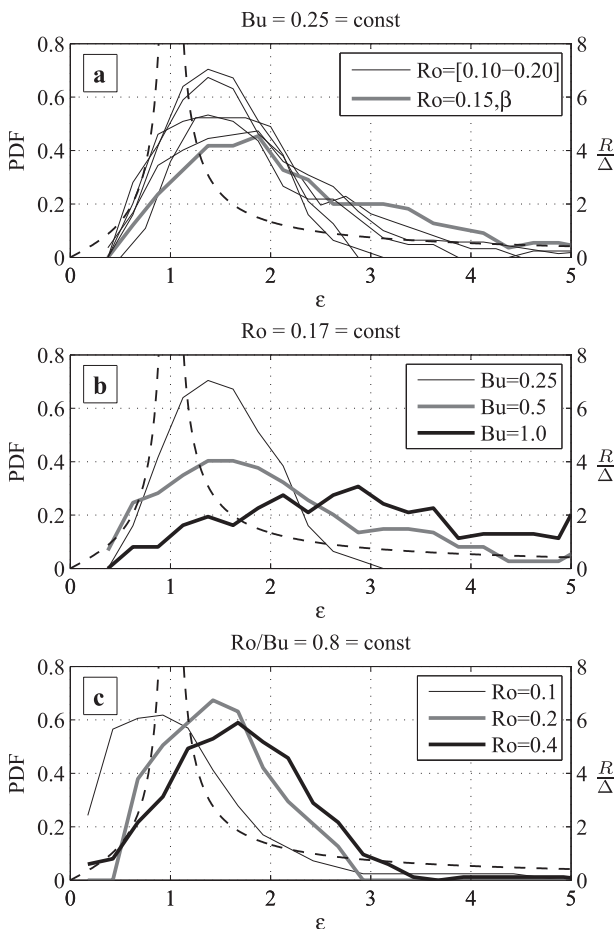


FIG. 10. PDF of ϵ (solid line; left y axis) for dipoles generated from different initial frontal configurations: (a) experiments 1–6; (b) experiments 5, 7, and 8; and (c) experiments 6, 9, and 10 (Table 1). The dashed lines in each panel (right y axis) show the dependence of dipole trajectory radius on ϵ .

a larger number of dipoles with dominant surface cyclones; the PDF of ϵ has a fatter tail and a peak shifted toward higher values (Fig. 10b; i.e., the probability of generating balanced dipoles is reduced). In the first set of experiments (Fig. 10a), the increase in H_1 (with $H_1 + H_2$ fixed) also produced stronger anticyclones, but the ϵ ratio was not significantly affected because stronger cyclones (resulting from a faster, deeper jet) were produced in layer 1 at the same time.

Motivated by these results, we explore further configurations with high Ro/Bu ratios [$Ro/Bu = H_1/(H_1 + H_2) = 0.8$; experiments 6, 9, and 10, Table 1] corresponding to anticyclones formed by strongly squeezing deep mixed layer waters into a thin layer as water parcels subduct across the front; such fronts generate relatively strong anticyclones. In this class of fronts, we investigate ϵ statistics for shallow/weak fronts ($H_1 = 20$ m, $H_2 = 5$ m,

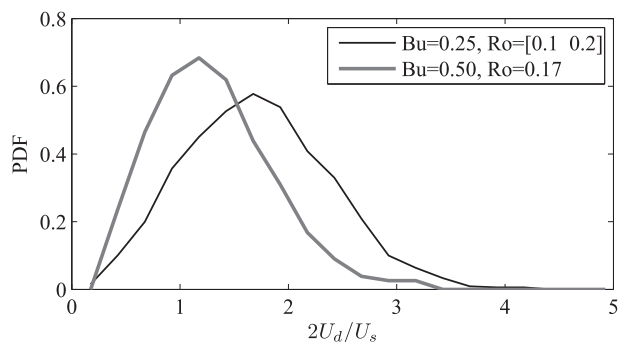


FIG. 11. PDF of twice the ratio of U_d to U_s for a range of initial frontal configurations (Table 1). The U_s is estimated by the same procedure as for Fig. 4b.

and $Ro = 0.1$) compared to deep/strong fronts ($H_1 = 80$ m, $H_2 = 20$ m, and $Ro = 0.4$). A shift to lower values of the peak of the PDF of ϵ and a reduction of the high- ϵ tail are observed for shallower fronts, both of which lead to a slightly increased probability p of balanced dipoles (Fig. 10c). For this frontal configuration, however, p remains small (similar to Fig. 9b).

These sensitivity estimations indicate that balanced dipoles are generated across a wide range of frontal configurations, with varying but nonnegligible probability. Nonetheless, not all balanced dipoles escape the influence of a slumping front; most of them do not self-propagate sufficiently fast to evade merger and recirculation processes. We thus assess the distribution of dipole drift speed U_d with respect to frontal-slumping speed U_s (Fig. 11). The requirement for dipole escape is $U_d > U_s/2$. The peak in the distribution is around 1 for all runs; as expected, a large fraction of dipoles have drift speeds that are comparable to frontal-slumping speeds because it is the dipoles themselves that influence frontal slumping. It is important to keep in mind that U_d is only in the direction of U_s in the early stages of dipole motion. Among the different frontal configurations, the distribution of U_d/U_s has a strong dependency on Bu (Ro is constant), with faster relative dipole speeds for smaller Bu , which is partially due to coupling between the layers that scales as $1/Bu$. Similar to the ϵ distribution, there is only a weak dependence on Ro (Bu is constant). Where Ro/Bu is constant, small Ro fronts tend to generate more dipoles with faster relative speeds. The initial frontal conditions that favor fast-moving dipoles are in agreement with those that generate more balanced dipoles ($\epsilon \approx 1$). This is partially because the two statistics are not independent [i.e., $U_d = 2U_2/(1 + \epsilon)$ implies that for fixed cyclone strengths strongly curved dipole trajectories ($\epsilon > 1$) also have smaller drift speeds].

Dipoles transport potential vorticity and buoyancy anomalies across the front and affect frontal-slumping

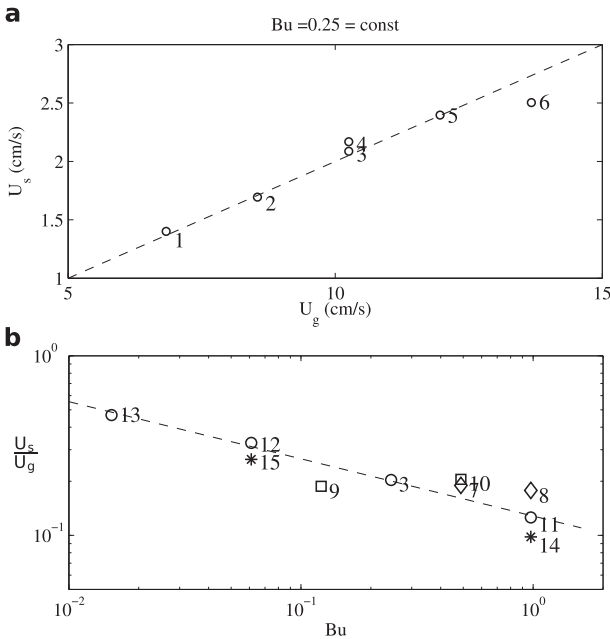


FIG. 12. (a) Frontal-slumping speed as a function of initial geostrophic velocity of the front for simulations with constant Bu (experiments 1–6, with 4 having nonzero β). The dashed line corresponds to $U_s = 0.2U_g$. (b) Nondimensional frontal-slumping speed U_s/U_g as a function of Bu for different experiments (experiment numbers as in Table 1 are annotated). The dashed line represents the $Bu^{-0.4}$ scaling.

speeds in a complicated manner—there exists a wide range of kinematic trajectories that are constrained by the statistics of ϵ and U_d/U_s . Spall and Chapman (1998) estimated the frontal-slumping speed to be related to the drift speed of a typical dipole, assuming that dipoles move perpendicular to the front. Curved dipole trajectories would imply decreased efficiency of frontal slumping. We next examine this effect by investigating frontal-slumping speeds for a range of initial frontal configurations.

For a constant Bu number (frontal width $L_f = 10$ km; experiments 1–6, Table 1), after the initial adjustment the front slumps with almost constant speed proportional to its initial geostrophic velocity $U_g \sim (g\Delta\rho_y H_1)/(f\rho_0 L_f)$ (Fig. 12a). The speed of frontal slumping does not appear to be significantly affected by the β effect. Simulations with wider initial frontal width L_f show a qualitatively different evolution (Fig. 13). Initially, instabilities develop everywhere within the wide front with eddies having small scales (Fig. 13a). These short unstable waves are of a mixed Rossby–Kelvin type and tend to alter the PV anomaly distribution before the onset of baroclinic instability (see, e.g., Morel et al. 2006; Gula et al. 2009; Sakai 1989). At later times, wide fronts sharpen owing to active frontogenesis (see, e.g., Pollard

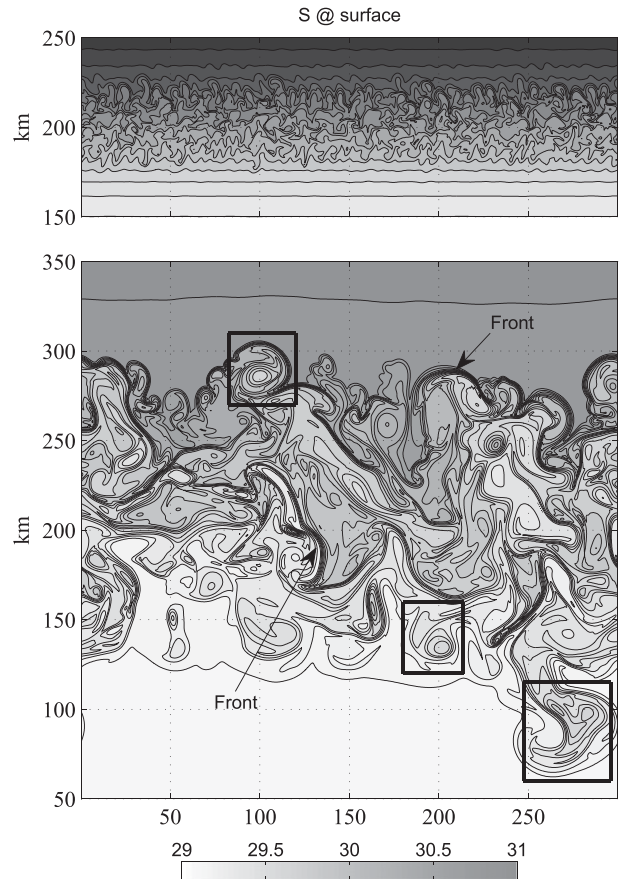


FIG. 13. (top) Surface salinity contours for a wide front at day 30 showing the presence of multiple small-scale eddies within the front (experiment 13, Table 1). (bottom) The surface salinity field at day 140. Note the presence of multiple fronts (arrows) separating waters of different salinities; sample dipoles are shown in black boxes.

and Regier 1992; Lapeyre et al. 2006), which leads to the formation of multiple narrow fronts separating intermediate water masses that originate within the initial front (Fig. 13b). Strong surface fronts are evident at the outer boundaries of the frontal region (north and south edges), with several weaker fronts present in between. Dipoles are commonly observed, particularly at the strongest north and south edge fronts; however, it is not possible within the formalism here to characterize dipole properties and trajectories within the wide frontal region.

The frontal width for initially thick fronts increases faster than for thin fronts and scales as $U_s/U_g \sim Bu^{-0.4}$ (Fig. 12b); varying the reduced gravity g'_1 (experiments 14 and 15, Table 1) has the similar effect on frontal-slumping speed as varying the frontal width L_f . The faster slumping speed for thick fronts is consistent with active frontogenesis, which effectively strengthens the

local geostrophic currents and produces stronger dipoles. The reduction in slumping speed with increased Bu is consistent with the experiment set shown in Fig. 10b, indicating a shift to higher ϵ (and therefore strongly curved dipole trajectories) with higher Bu. The link between decreased slumping efficiency for increased Bu and more curved dipole trajectories, however, is complicated by the effects of dipole interactions with other eddies and frontal meanders. The relation between the strength of the frontal slumping to dipole ϵ and $U_{d1}U_s$ distributions remains an open question.

7. Discussion and summary

We have simulated instabilities at a surface ocean front that grow to form eddies—in particular, dipoles that can self-propagate away from the widening front. As the front spins down, the numerical model runs show a clear inverse energy cascade through which eddies of the same vorticity sign merge as they become sufficiently close to each other. In general, this eddy field constitutes the slumping front, although some dipoles become separated from the front and evolve without frontal influences. To remain separated, dipoles must propagate away from the front faster than the frontal-slumping speed to avoid interactions and mergers that lead to their reincorporation into the front.

A closed analytical solution has been derived for the ratio ϵ of the translation velocities of a dipole based on the PV anomalies of its cyclone and anticyclone. We have further related ϵ to the radius of a self-propagating dipole trajectory, where a large propagation radius is found when $\epsilon \rightarrow 1$. Our theoretical results provide guidance in interpreting numerical model results. Analysis of dipoles from an ensemble of numerical simulations allows us to obtain statistical properties of dipoles and identify how they change for different frontal configurations. The ϵ distribution has a long high ϵ tail implying strongly curved trajectories because of the dominance of the cyclone in a dipole. The ϵ distribution has only weak dependence on the frontal Ro number and a stronger dependence on the Bu number such that shallow fronts with a large Ro/Bu ratio are more favorable to the production of balanced dipoles, although this probability is consistently small (about 20%). We observe only balanced dipoles to escape the influence of the front, although not all balanced dipoles escape as they are subject to interaction with frontal meanders and other dipoles. Understanding frontal slumping and property transports in the vicinity of fronts is complicated by curved dipole trajectories that lead to recirculation of buoyancy.

The result that the probability of balanced dipole generation is small may be inconsistent with persistent

observations of many upper-ocean eddies in the Arctic, if indeed they do translate far from the front as self-propagating dipoles. This suggests that in nature there might exist a mechanism acting to increase the probability of dipole escape. For example, nonuniform or time-dependent frontal characteristics may increase the probability of dipole escape. Such fronts could be intermittently unstable, or unstable only in localized areas, which allows for the production of dipole patches separated in time or spatially, thus reducing eddy–eddy interactions. Intermittent or localized dipole production could be related to transient frontal instabilities triggered by wind bursts or localized buoyancy forcing. Note that in a case where PV is not conserved, Thomas et al. (2008) examines the formation of intrathermocline eddies at upper-ocean fronts that are forced by winds. He shows the importance of down-front winds in driving a three-dimensional circulation that subducts surface water of low PV into the stratified interior. Such processes that influence the strengths of cyclone and anticyclone could shift the ϵ distribution toward more balanced values.

While we have put forward dipole self-propagation as a mechanism for eddy propagation from a front, there remains the possibility that background flow could advect eddies away from their originating front, and self-propagation is not required. In the case of Arctic eddies, for example, one could argue that they are advected in the large-scale Beaufort Gyre circulation (see, e.g., Proshutinsky et al. 2009; Spall et al. 2008), although for the class of arctic eddies discussed here the flow field to the south of the originating front is likely to be predominantly in the direction of the front. Moreover, for background advection to have a significant influence on the eddy pathway, it is necessary to first generate an eddy that is separated from the influence of the front and other eddies. A similar logic applies to the idea of vortex drift due to β effects.

Finally, we note that only sub-mixed layer anticyclones are persistently detected (i.e., no cyclones) in the observations of shallow eddies in the Arctic Ocean, with a few observations of dipoles under sea ice (e.g., Fedorov and Ginsburg 1989). If dipole self-propagation is important, cyclones are also required. It is a reasonable assumption, however, that dipoles are formed, and after some time, the surface-intensified cyclonic eddy is dissipated due to Ekman layers associated with under sea ice friction. The sub-mixed layer anticyclone remains largely unaffected by surface processes owing to a stratification cap at the base of the mixed layer. A similar dissipation process has been investigated for dipoles generated by convection under sea ice (e.g., Chao and Shaw 1999), where it has been shown that the surface

cyclone dissipates while the underlying anticyclone is preserved. Of course, the dissipation of a surface cyclone would affect the trajectory of a dipole and its propagation speed (e.g., Sansón et al. 2001). As the cyclone dissipates, the dipole loses the ability to self-propagate; the distance traveled by a dipole then depends strongly on surface frictional processes (e.g., sea ice cover state), and this is the subject of a future study.

Acknowledgments. This work was supported in part by the facilities and staff of the Yale University Faculty of Arts and Sciences High Performance Computing Center and by the National Science Foundation under Grant #CNS 08-21132 that partially funded acquisition of the facilities. Funding was also provided by the National Science Foundation Office of Polar Programs Arctic Sciences Section under Award ARC-1107623. We thank Woosok Moon and Andrew Wells for discussions on the analytical model, Claudia Cenedese for hosting a laboratory experiment for our further studies, and Leif Thomas for comments on the numerical model setup. Comments from two anonymous reviewers that lead to improvements in the paper were greatly appreciated.

APPENDIX

2½-Layer Quasigeostrophic Model of a Dipole

a. Point vortices

We first consider point vortices and later include more realistic Gaussian vortices. The leading-order approximation to dipole dynamics can be recovered from the linear 2½-layer quasigeostrophic equations (Pedlosky 1982), assuming that PV anomalies for each of the vortices as well as their separation distance Δ are known:

$$\nabla^2\psi_1 + F_1(\psi_2 - \psi_1) = S_1\delta(\mathbf{r}) \quad \text{and} \quad (\text{A1})$$

$$\nabla^2\psi_2 + F_2(\psi_1 - \psi_2) - F_3\psi_2 = S_2\delta(\mathbf{r} - \Delta). \quad (\text{A2})$$

The streamfunctions in layers 1 and 2 are $\psi_{1,2}$; the stratification parameters [(15)] are $F_{1,2,3}$; and the dipole PV anomalies multiplied by mean layer thickness in corresponding layers are $S_{1,2}$. Layer 2 has a PV anomaly that is offset by a distance Δ with respect to the center of the PV anomaly in layer 1. This introduces an asymmetry in an otherwise axisymmetric setup. However, the solution to the linear equations can be split into a sum of two: one only has a PV anomaly in layer 1 and another only has a PV anomaly in layer 2. The two solutions obey the same equation set, with the difference in the source terms:

$$\nabla^2\psi_1 + F_1(\psi_2 - \psi_1) = S_1\delta(r) \quad \text{and} \quad (\text{A3})$$

$$\nabla^2\psi_2 + F_2(\psi_1 - \psi_2) - F_3\psi_2 = S_2\delta(r), \quad (\text{A4})$$

now in terms of polar coordinate r , where in one solution we set $S_1 = 0$ and in another $S_2 = 0$. This linear system of coupled equations can be decoupled into two independent vertical mode equations

$$\nabla^2\Psi_{1,2} - c_{1,2}\Psi_{1,2} = Q_{1,2} \quad (\text{A5})$$

using a linear substitution $\Psi_{1,2} = (F_2 + F_3 - c_{1,2})\psi_1 + F_1\psi_2$ where $Q_{1,2}$ is the source term (linear combination of S_1 and S_2) and $c_{1,2}$ are two positive constants defined as

$$c_{1,2} = \frac{F_1 + F_2 + F_3}{2} \pm \sqrt{\frac{(F_1 + F_2 + F_3)^2}{4} - F_1F_3}. \quad (\text{A6})$$

The equations for Ψ are identical to a 1½-layer quasigeostrophic system with $c = 1/\lambda^2$ being a stratification parameter corresponding to the internal deformation radius λ for this mode. We thus split the equations into two modes (first and second baroclinic modes) to obtain

$$\nabla^2\Psi_1 - 1/\lambda_1^2\Psi_1 = [(F_2 + F_3 - c_1)S_1 + F_1S_2]\delta(r) \quad \text{and} \quad (\text{A7})$$

$$\nabla^2\Psi_2 - 1/\lambda_2^2\Psi_2 = [(F_2 + F_3 - c_2)S_1 + F_1S_2]\delta(r). \quad (\text{A8})$$

These are the modified Bessel equations for which fundamental solutions bounded at infinity are the modified Bessel functions K_0 :

$$\Psi_1 = [(F_2 + F_3 - c_1)S_1 + F_1S_2]K_0(r/\lambda_1) \quad \text{and} \quad (\text{A9})$$

$$\Psi_2 = [(F_2 + F_3 - c_2)S_1 + F_1S_2]K_0(r/\lambda_2). \quad (\text{A10})$$

The original variables are recovered by the inverse transformation:

$$\psi_1 = -\frac{\Psi_1 - \Psi_2}{c_1 - c_2} \quad \text{and} \quad (\text{A11})$$

$$\psi_2 = -\frac{\Psi_1(F_2 + F_3 - c_2) - \Psi_2(F_2 + F_3 - c_1)}{F_1(c_1 - c_2)}. \quad (\text{A12})$$

Next we consider the two cases, each with a PV anomaly in only one of the layers. In the first case with $S_2 = 0, S_1 \neq 0$,

$$\Psi_1 = S_1(F_2 + F_3 - c_1)K_0(r/\lambda_1) \quad \text{and} \quad (\text{A13})$$

$$\Psi_2 = S_1(F_2 + F_3 - c_2)K_0(r/\lambda_2). \quad (\text{A14})$$

In this case, the layer-1 vortex induces a circulation in layer 2, which advects the vortex in layer 2 and

$$\psi_2 = S_1 F_2 \frac{K_0(r/\lambda_1) - K_0(r/\lambda_2)}{c_2 - c_1}, \quad (\text{A15})$$

because $(F_2 + F_3 - c_1)(F_2 + F_3 - c_2) = -F_1 F_2$.

In the second case with $S_2 \neq 0$, $S_1 = 0$,

$$\Psi_1 = S_2 F_1 K_0(r/\lambda_1) \quad \text{and} \quad (\text{A16})$$

$$\Psi_2 = S_2 F_1 K_0(r/\lambda_2). \quad (\text{A17})$$

In this case, the layer-2 vortex induces a circulation in layer 1, which advects the vortex in layer 1 and

$$\psi_1 = S_2 F_1 \frac{K_0(r/\lambda_1) - K_0(r/\lambda_2)}{c_1 - c_2}. \quad (\text{A18})$$

Given the velocity fields induced by each of the vortices, the propagation speeds of the vortex centers can be deduced

$$U_i = u_i|_{r=\Delta} = \frac{\partial \psi_i}{\partial r} \Big|_{r=\Delta}, \quad i = 1, 2. \quad (\text{A19})$$

Because ψ_1 and ψ_2 have the same functional form, we can easily obtain the important ratio $\epsilon = U_2/U_1$, which determines the radius of the dipole trajectory:

$$\epsilon = \frac{S_1 F_2}{S_2 F_1} = \frac{S_1 H_1}{S_2 H_2}. \quad (\text{A20})$$

b. Gaussian vortices

The derivations found in the previous section provide a Green's function for the vortex streamfunction, which can be used to recover the circulation of a vortex with an arbitrary shape of PV anomaly. One could obtain it by taking a convolution of the Green's function with a source term, which requires evaluating a two-dimensional integral. In the case of axisymmetric vortices with a Gaussian PV distribution (a good approximation to the eddies observed in the simulations), the problem can be simplified through the use of the Hankel transformation:

$$\hat{\Psi}(k) = \int_0^\infty \Psi(r) J_0(kr) r dr \quad \text{and} \quad (\text{A21})$$

$$\Psi(r) = \int_0^\infty \hat{\Psi}(k) J_0(kr) k dk, \quad (\text{A22})$$

where J_0 is a zero-order Bessel function of the first kind (Abramowitz and Stegun 1972). We use a Gaussian profile for the source term $Q = Q_0 \exp(-r^2/2\sigma^2)$, where parameters Q_0 and σ are obtained by the best fit to PV anomalies in corresponding layers (Fig. 8a). Note that after splitting equations into contributions from individual eddies the source term Q is proportional to either S_1 or S_2 (not their linear combination), thus preserving the Gaussian form. Applying the Hankel transform to (A5) (and dropping subscripts 1 and 2) we obtain a solution in k space:

$$\hat{\Psi} = -\frac{\hat{Q}}{k^2 + c}, \quad (\text{A23})$$

where $\hat{Q}(k) = Q_0 \sigma^2 \exp(-k^2/2\sigma^2)$. The solution in r space is expressed in the form of a one-dimensional integral

$$\Psi(r) = -Q_0 \sigma^2 \int_0^\infty \frac{\exp\left(-\frac{k^2 \sigma^2}{2}\right)}{k^2 + c} J_0(kr) k dk, \quad (\text{A24})$$

which is evaluated numerically. A linear inverse transformation [(A11) and (A12)] to original variables is then applied and the azimuthal velocity fields are calculated as derivatives of the streamfunctions (as in the case of point vortices).

The procedure allows us to separate the velocity field in a dipole into contributions from individual eddies and thus obtain the self-advecting velocities $U_{1,2}$. The propagating velocity of the surface cyclonic vortex U_1 is calculated as the velocity generated by the anticyclonic vortex (u_1) at the location of the core of the cyclonic vortex and vice versa. We calculate U_1 as $u_1(r)$ averaged over the interval $[\Delta - \sigma, \Delta + \sigma]$ (where square brackets denote an interval of values on a real axis).

REFERENCES

- Abramowitz, M., and I. Stegun, 1972: *Handbook of Mathematical Functions with Formulas, Graphs, and Mathematical Tables*. Dover Publications, 1046 pp.
- Adcroft, A., and Coauthors, 2013: *MITgcm User Manual*. MIT Department of EAPS, 464 pp.
- Ahl nas, K., T. C. Royer, and T. H. George, 1987: Multiple dipole eddies in the Alaska Coastal Current detected with Landsat thematic mapper data. *J. Geophys. Res.*, **92** (C12), 13 041–13 047.
- Boccaletti, G., R. Ferrari, and B. Fox-Kemper, 2007: Mixed layer instabilities and restratification. *J. Phys. Oceanogr.*, **37**, 2228–2250.
- Carton, X., 2001: Hydrodynamical modeling of oceanic vortices. *Surv. Geophys.*, **22**, 179–263.
- , 2010: Oceanic vortices. *Lect. Notes Phys.*, **805**, 61–108.

- Chao, S.-Y., and P.-T. Shaw, 1999: Close interactions between two pairs of heton-like vortices under sea ice. *J. Geophys. Res.*, **104** (C10), 23 591–23 605.
- Chelton, D. B., M. G. Schlax, and R. M. Samelson, 2011: Global observations of nonlinear mesoscale eddies. *Prog. Oceanogr.*, **91**, 167–216.
- Chérubin, L., X. Carton, and D. G. Dritschel, 2007: Vortex dipole formation by baroclinic instability of boundary currents. *J. Phys. Oceanogr.*, **37**, 1661–1677.
- Couder, Y., and C. Basdevant, 1986: Experimental and numerical study of vortex couples in two-dimensional flows. *J. Fluid Mech.*, **173**, 225–251.
- de Ruijter, W. P., H. M. v. Aken, E. J. Beier, J. R. Lutjeharms, R. P. Matano, and M. W. Schouten, 2004: Eddies and dipoles around south Madagascar: Formation, pathways and large-scale impact. *Deep-Sea Res. I*, **51**, 383–400.
- Eady, E. T., 1949: Long waves and cyclone waves. *Tellus*, **1**, 33–52.
- Fedorov, K. N., and A. I. Ginsburg, 1989: Mushroom-like currents (vortex dipoles): One of the most widespread forms of non-stationary coherent motions in the ocean. *Mesoscale/Synoptic Coherent Structures in Geophysical Turbulence*, J. C. J. Nihoul and B. M. Jamart, Eds., Elsevier Oceanographic Series, Vol. 50, Elsevier, 1–14.
- Flierl, G. R., 1987: Isolated eddy models in geophysics. *Annu. Rev. Fluid Mech.*, **19**, 493–530.
- , V. D. Larichev, J. C. McWilliams, and G. M. Reznik, 1980: The dynamics of baroclinic and barotropic solitary eddies. *Dyn. Atmos. Oceans*, **5**, 1–41.
- , M. E. Stern, and J. A. Whitehead, 1983: The physical significance of modons: Laboratory experiments and general integral constraints. *Dyn. Atmos. Oceans*, **7**, 233–263.
- Fox-Kemper, B., R. Ferrari, and R. Hallberg, 2008: Parameterization of mixed layer eddies. Part I: Theory and diagnosis. *J. Phys. Oceanogr.*, **38**, 1145–1165.
- Gryanik, V. M., 1983: Dynamics of singular geostrophic vortices in a two-layer model of the atmosphere (ocean). *Izv. Atmos. Ocean. Phys.*, **19**, 227–240.
- , M. A. Sokolovskiy, and J. Verron, 2006: Dynamics of heton-like vortices. *Regular Chaotic Dyn.*, **11**, 383–434.
- Gula, J., R. Plougonven, and V. Zeitlin, 2009: Ageostrophic instabilities of fronts in a channel in a stratified rotating fluid. *J. Fluid Mech.*, **627**, 485.
- Herbette, S., Y. Morel, and M. Arhan, 2004: Subduction of a surface vortex under an outcropping front. *J. Phys. Oceanogr.*, **34**, 1610–1627.
- Hogg, N., and H. Stommel, 1985: The heton, an elementary interaction between discrete baroclinic geostrophic vortices, and its implications concerning eddy heat-flow. *Proc. Roy. Soc. London*, **A397**, 1–20.
- Killworth, P. D., 1983: On the motion of isolated lenses on a β plane. *J. Phys. Oceanogr.*, **13**, 368–376.
- Krishfield, R., J. Toole, A. Proshutinsky, and M.-L. Timmermans, 2008: Automated ice-tethered profilers for seawater observations under pack ice in all seasons. *J. Atmos. Oceanic Technol.*, **25**, 2091–2095.
- Lapeyre, G., P. Klein, and B. L. Hua, 2006: Oceanic restratification forced by surface frontogenesis. *J. Phys. Oceanogr.*, **36**, 1577–1590.
- Lee, C., L. Thomas, and Y. Yoshikawa, 2006: Intermediate water formation at the Japan/East Sea subpolar front. *Oceanography*, **19**, 110–121.
- Legg, S., and J. Marshall, 1993: A heton model of the spreading phase of open-ocean deep convection. *J. Phys. Oceanogr.*, **23**, 1040–1056.
- , H. Jones, and M. Visbeck, 1996: A heton perspective of baroclinic eddy transfer in localized open ocean convection. *J. Phys. Oceanogr.*, **26**, 2251–2266.
- Morel, Y., and J. McWilliams, 2001: Effects of isopycnal and diapycnal mixing on the stability of oceanic currents. *J. Phys. Oceanogr.*, **31**, 2280–2296.
- , D. S. Darr, and C. Talandier, 2006: Possible sources driving the potential vorticity structure and long-wave instability of coastal upwelling and downwelling currents. *J. Phys. Oceanogr.*, **36**, 875–896.
- Nof, D., 1981: On the β -induced movement of isolated baroclinic eddies. *J. Phys. Oceanogr.*, **11**, 1662–1672.
- Pedlosky, J., 1982: *Geophysical Fluid Dynamics*. Springer-Verlag, 636 pp.
- , 1985: The instability of continuous heton clouds. *J. Atmos. Sci.*, **42**, 1477–1486.
- Pollard, R. T., and L. A. Regier, 1992: Vorticity and vertical circulation at an ocean front. *J. Phys. Oceanogr.*, **22**, 609–625.
- Polvani, L., 1991: Two-layer geostrophic vortex dynamics. Part 2: Alignment and two-layer V-states. *J. Fluid Mech.*, **225**, 241–270.
- Proshutinsky, A., and Coauthors, 2009: Beaufort Gyre freshwater reservoir: State and variability from observations. *J. Geophys. Res.*, **114**, C00A10, doi:10.1029/2008JC005104.
- Reinaud, J. N., and X. Carton, 2009: The stability and the nonlinear evolution of quasi-geostrophic hetons. *J. Fluid Mech.*, **636**, 109–135.
- Rhines, P. B., 1979: Geostrophic turbulence. *Annu. Rev. Fluid Mech.*, **11**, 401–441.
- Saffman, P. G., 1992: *Vortex Dynamics*. Cambridge University Press, 328 pp.
- Sakai, S., 1989: Rossby–Kelvin instability: A new type of ageostrophic instability caused by a resonance between Rossby waves and gravity waves. *J. Fluid Mech.*, **202**, 149–176.
- Sansón, L. Z., G. J. F. van Heijst, and N. A. Backx, 2001: Ekman decay of a dipolar vortex in a rotating fluid. *Phys. Fluids*, **13**, 440, doi:10.1063/1.1335541.
- Smith, K., and G. Vallis, 2001: The scales and equilibration of midocean eddies: Freely evolving flow. *J. Phys. Oceanogr.*, **31**, 554–571.
- Sokolovskiy, M. A., and J. Verron, 2000: Finite-core hetons: Stability and interactions. *J. Fluid Mech.*, **423**, 127–154.
- Spall, M. A., 1995: Frontogenesis, subduction, and cross-front exchange at upper-ocean fronts. *J. Geophys. Res.*, **100** (C2), 2543–2557.
- , and D. Chapman, 1998: On the efficiency of baroclinic eddy heat transport across narrow fronts. *J. Phys. Oceanogr.*, **28**, 2275–2287.
- , R. S. Pickart, P. S. Fratantoni, and A. J. Plueddemann, 2008: Western Arctic shelfbreak eddies: Formation and transport. *J. Phys. Oceanogr.*, **38**, 1644–1668.
- Stern, M. E., and J. A. Whitehead, 1990: Separation of a boundary jet in a rotating fluid. *J. Fluid Mech.*, **217**, 41–69.
- Stone, P. H., 1966: On nongeostrophic baroclinic stability. *J. Atmos. Sci.*, **23**, 390–400.
- Swaters, G. E., 1995: Mathematical modelling of solitary oceanographic vortices. *Fluid Vortices*, Springer, 575–615.
- Thomas, L. N., 2008: Formation of intrathermocline eddies at ocean fronts by wind-driven destruction of potential vorticity. *Dyn. Atmos. Oceans*, **45**, 252–273.
- , A. Tandon, and A. Mahadevan, 2008: Sub-mesoscale processes and dynamics. *Ocean Modeling in an Eddy*

- Regime, Geophys. Monogr.*, Vol. 177, Amer. Geophys. Union, 17–38.
- Timmermans, M.-L., J. Toole, A. Proshutinsky, R. Krishfield, and A. Plueddemann, 2008: Eddies in the Canada Basin, Arctic Ocean, observed from ice-tethered profilers. *J. Phys. Oceanogr.*, **38**, 133–145.
- Toole, J., R. Krishfield, M.-L. Timmermans, and A. Proshutinsky, 2011: The ice-tethered profiler: Argo of the arctic. *Oceanography*, **24**, 126–135, doi:10.5670/oceanog.2011.64.
- Vallis, G. K., 2006: *Atmospheric and Oceanic Fluid Dynamics*. Cambridge University Press, 745 pp.
- van Heijst, G. J. F., and J. B. Flor, 1989: Dipole formation and collisions in a stratified fluid. *Nature*, **340**, 212–215.
- , and H. J. H. Clercx, 2009: Laboratory modeling of geophysical vortices. *Annu. Rev. Fluid Mech.*, **41**, 143–164.
- Voropayev, S. I., Y. D. Afanasyev, and I. A. Filippov, 1991: Horizontal jets and vortex dipoles in a stratified fluid. *J. Fluid Mech.*, **227**, 543–566.